Measurements of Double K-shell ionization in Mn-54, Zn-65 and Fe-55

Master's Thesis in Physics

Presented by
Daniel Voigt
August 27,2018

Erlangen Centre for Astroparticle Physics
Physikalisches Institut IV
Friedrich-Alexander-Universität Erlangen-Nürnberg

Supervisor: Dr. Thilo Michel

Contents

1 Introduction

It is well known how in electron capture or photoionization processes single vacancies can be developed in the K-shell of an atom. Double vacancy creation in the K-shell as a result of such an ionization process however only recently piqued the interest of the scientific community. These 'hollow atoms', atoms with an empty K-shell, but fully occupied higher shells, have a lifetime of only few hundreds of femtoseconds. Electrons from higher atom shells are quick to fill the two K-shell vacancies, emmitting X-ray fluorescences in the process. The existence of two vacancies or susbsequently one vacancy alters energy levels of the atom, so that the first X-ray fluorescence, labelled 'satellite', and the second X-ray fluorescence, labelled 'hypersatellite', have slightly differing but distinct energies.
The possibility of measuring satellites and hypersatellites resulted in numerous measurements and theoretical analysis from various groups [1] [2] [3]. The Primakoff-Porter theory [4] attempts to explain the relation between probability of double K-Shell vacancy and atom number. However, this theory is partially in disagreement with experimental results. There are results confirming different modells [5] and many questions remain open.
The motivation for this work is therefore to further the landscape of available data and understanding the problems, measurements of double K-Shell vacancy production can face.
In this work, the probability of double K-Shell vacancy creation is measured for the electron capture of the elements of Mn-54, Zn-65 and Fe-55. To achieve that, coincidence measurements of K-fluorescences were taken using a setup of Timepix3 detectors. The cases of Mn-54 and Zn-65 experience internal conversion effects. Since the result, a double K-Shell vacancy, is the same as the process to be observed, the energy signature is similar. To resolve this effect, the internal conversion coefficient was measured for these elements and a 3-coincidence measurement, consisting of two K-Fluorescences and one gamma particle, was made.

2 Theory

The following chapter will discuss theoretical backgrounds necessary for understanding the measurements. Most notably, the theory of Double K-Shell ionisation and the structure of the Timepix3-Detectors will be discussed.

2.1 Double K-Shell ionisation

Double K-Shell ionisation is a process which occurs aside production of single K-Shell vacancies. The probability for Double K-Shell vacancy creation, denoted P_{KK} is in the order of $10^{-5} - 10^{-4}$, depending on the atomic number Z. This effect occurs during electron capture.
The processes responsible for this effect are called ' shake processes '. Shake processes occur, when a fast electron leaves the atom shell. Due to relaxation of the atom, the second K-shell electron can be ' shaken up ' to a higher atom shell or even ' shaken off ' out of the atom.
To investigate this effect it is possible to observe resulting K-Fluorescences. Since the empty K-Shell will be occupied by electrons of higher energy levels, the difference will be emitted as X-ray photons. The emission will happen upon reoccupation of the vacancy with a probability ω_K called the ' fluorescence yield '. Is the K-shell empty, the energies of these fluorescences will be shifted to higher energies. The fluorescence emitted upon occupation of the first vacancy is called ' hypersatellite ' with a fluorescence yield denoted as ω_K^{HS}. The fluorescence resulting from occupation of the second vacancy is called ' satellite ' with a fluorescence yield ω_K^S. The energy of the satellite is also shifted to higher energies, since a spectator vacancy in a higher shell was created at reoccupation of the first K-shell vacancy.
The P_{KK} depends on the element used. As a function of the atomic number Z P_{KK} follows a power law, as depicted in 2.1.
With the setup used in this work, there are two ways to measure P_{KK}. One involves the measurement of two coincident K-Fluorescences, to indicate a hollow atom, with subsequent subtraction of the internal conversion probability (For further

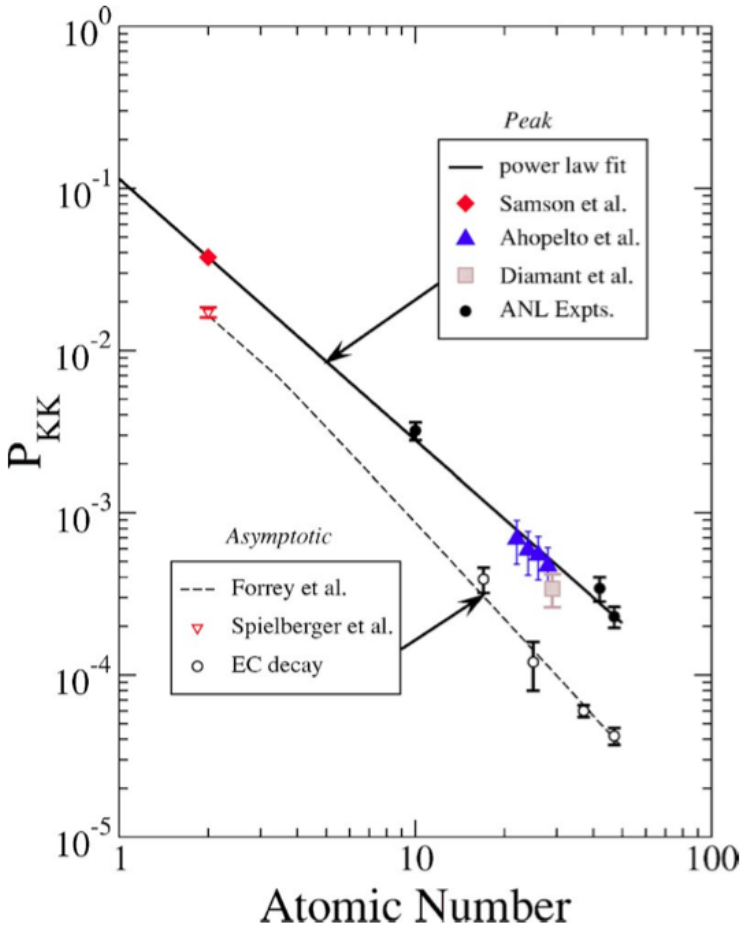

Figure 2.1: *Distribution of P_{KK} over atomic number Z. Pictured are several measurements, as well as a power law fit, highlighting the relation of P_{KK} to atom number Z. Graphic and sources for measurements from [6].*

information on internal conversion, refer to section 2.3). The other way eliminates this subtraction by measuring two coincident K-Fluorescences in addition to a third coincident event in form of a transition gamma. In case such a 3-coincidence is observed, the transition gamma could not have produced an internal conversion electron and true double K-shell ionization took place.
The formulae for each method are described as:

$$P_{KK,2coinc} = \frac{N_{2KF} - N_{rand,2}}{\delta_{HS}\delta_S\omega_{HS}\omega_S AT} - \alpha_K \tag{2.1}$$

$$P_{KK,3coinc} = \frac{N_{2KF1\gamma} - N_{rand,3}}{\delta_{HS}\delta_S\delta_\gamma\omega_{HS}\omega_S\omega_{gamma} AT} \tag{2.2}$$

The occuring coefficients are defined as followed:

- $N_{rand,2}, N_{rand,3}$ are the backgrounds consisting of random coincident events for each of the measurement techniques. This background can be approximated by evaluating the time differences of coincident events and comparing ' true ' coincidences with less time difference to coincidences with a high time difference, as they are uncorrelated and truly random.
- $\delta_{HS}, \delta_S, \delta_\gamma$ are the detection efficiencies for hypersatellites (HS), satellites (S) and gamma transition events (γ). The detection efficiency describes the ability of the detector to measure an event. This ability can vary based on energy and nature of radiation. For example, since electrons have a higher scattering cross section in the detector material, they are more likely to be detected than gamma photons. The detection efficiency is defined as the ratio between measured events and expected events.
- ω_{HS}, ω_S are the fluorescence yields for hypersatellites and satellites. They describe the probability of a fluorescence to be emitted in case of recombination. ω_γ is similarily defined as the probabilty of a gamma photon to be emitted upon gamma transition.
- A describes the activity of the source at beginning of the measurement.
- T describes the duration of the measurement.
- α_K describes the internal conversion coefficient. For further information on nature, calculation and value refer to sections 2.3 and 5.3.

ω	Mn-54	Zn-65	Fe-55
ω_K	0.289	0.454	0.321
ω_S	0,339	0,532	0,377
ωHS	0,344	0,540	0,382
ω_γ	0.999997	0.5023	$--$

Table 2.1: *Fluorescence yields and gamma emission probability for Mn-54, Zn-65 and Fe-55. ω_S and ω_{HS} are taken from [2]. The related values for Zn-65 and Fe-55 are extrapolated through relation of these values to ω_K of Mn-54. ω_K values were taken from [7] [8] and [9].*

2.2 Timepix3

The Timepix3 detector is a pixelated hybrid and active semiconductor detector, capable of measuring location, time and energy information. As a rework of the Medipix3 detector, which is mainly used in medical applications, the Timepix3 proved to be useful in medicine as well as particle physics. It was designed and developed by the CERN Medipix collaboration.
The detectors used in this work possessed a pixelmatrix of 256×256 pixel.

2.2.1 Structure

The structure of the Timepix3 is similar to Timepix, depicted in figure 2.2. The semiconductor sensor layer is through bump bonding connected to the ASIC (application-specific integrated circuit).
The sensor itself consists of either Silicon or Cadmium-Telluride. The material dictates the polarity of the chip. The thickness of the sensor material depends on the application and material used. In this work a 500 μm thick Silicon layer was used as detector material.
Through bump bonding the pixelated structure of the ASIC gets connected to the uniform sensor layer, since every pixel yields a bump bonding connection. This hybrid construction allows for specific calibration of each pixel.
The ASIC is the readout electronic of the detector and yields the pixelated structure. In this work two detectors with each 256×256 pixel are used, each pixel having a pitch of $55\mu m$. The ASIC digitizes the signal and sends it for further processing

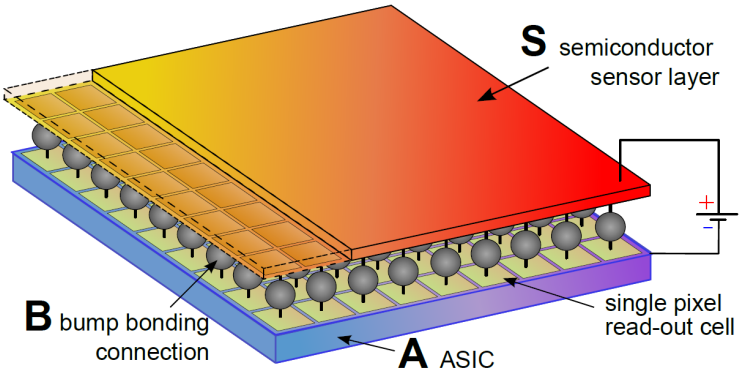

Figure 2.2: *Structure of a Timepix Chip. Depicted are the sensor layer with the bump bonding connection directly beneath. The bump bonds connect the sensor with the ASIC.*

to the external readout electronics (for further information about readouts used refer to section 3).

2.2.2 Detection

In the following section the detection process is explained. The main processes used to detect an ionizing particle are scattering processes. Upon interaction with the detector an ionizing particle transports some of its energy to electrons in the valence band of the semiconducting sensor layer. This increasal in energy leads the electron to rise into the conduction band, leaving a hole in the valence band. With this process the ionizing particle can create multiple thousands of such 'electron-hole pairs', forming a 'charge cloud'. The energy W necessary to create an electron-hole pair is described as:

$$W = E_i + f \cdot E_x + \bar{\epsilon} \tag{2.3}$$

E_i is the average ionization energy of the material, f is the average number of excited electron-hole pairs, E_x is the energy necessary to create an electron-hole pair and $\bar{\epsilon}$ describes the average kinetic energy of an electron-hole pair. As such, W is dependant on the material used as sensor layer. The average ionization energy of Silicon, as used in this work, is $E_i = 3.62eV$.

Upon creation of electron-hole pairs the charge carriers start drifting to the electrode of the detector according to an applied bias voltage. Either electrons or holes drift to the electrode, dependant on the polarity of the bias voltage. For Silicon, ususally the bias voltage gets chosen as such the holes are drifting. This drift process has two consequences: Recombination of charge carriers is prevented and a current occurs. This current gets integrated over an 'acquisition time' and converted into a voltage pulse. The length of this voltage pulse is proportional to the number of charge carriers produced and as such proportional to the energy of the ionizing particle. The height of this voltage pulse is compared to an adjustable threshold value ('THL'). The length of the pulse, corresponding to the energy of the particle, is then described as the time of the voltage pulse above the THL ('Time over Threshold' or 'ToT').
The relation between ToT and energy is described as:

$$ToT(E) = a \cdot E + b - \frac{c}{E - t} \tag{2.4}$$

For calibration of the detectors and subsequent evaluation of the data, it is necessary to invert formula 2.4 and measure the parameters. The inverted relation is described as:

$$E(ToT) = \frac{a \cdot t + TOT - b + \sqrt{(b + a \cdot t - TOT)^2 + 4 \cdot a \cdot c}}{2 \cdot a} \tag{2.5}$$

2.2.3 Strengths and Flaws

As opposed to the previous iteration of Timepix detectors, the Timepix3 does not have to work in a frame-based acquisition mode [10] [11]. The pixel columns of the detector are continuously read out, each event labeled with a timestamp, so, given the boundaries of the detector internal clock, the time of arrival for every event is known ('ToA').
However, since pixel columns are read out at once, columns are also susceptible to errors. For example, it is not rare for a detector to have erronous ToA values throughout whole pixel rows. These effects stem from electronical faults within the clocks used to measure ToA. From this fault no effect on ToT measurements was observed. An example of this effect is depicted in figure 2.3.
One problem stemming from the pixelated and hybrid structure of the detector is called 'Charge Sharing', depicted in figure 2.4. During the drift of the charge carriers, diffusion takes place, leading to the charge cloud dissipating. If large

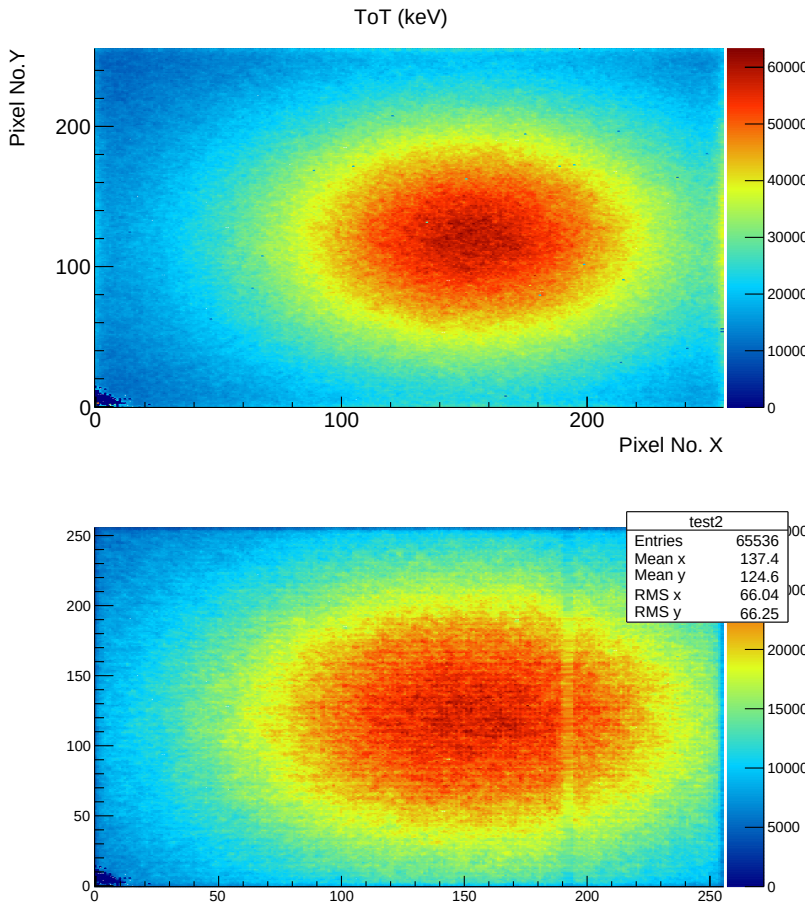

Figure 2.3: *Spatial ToT- and ToA-distributions (ToT: above; ToA: below) of a Mn-54 source with 10 hours exposure. The bug in columns 191 and 192 is only visible in ToA values.*

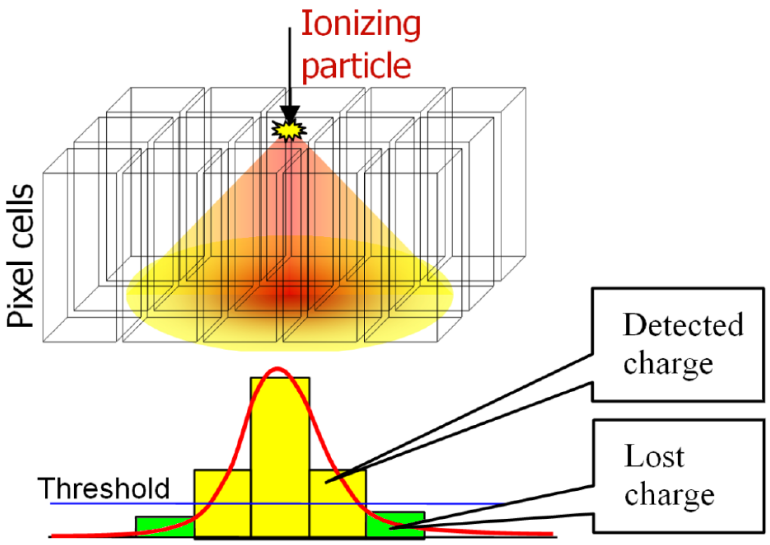

Figure 2.4: *Depiction of the Charge Sharing Effect. The electron cloud is diffusing on its way to the electrode. The diffusion can lead over to neighboring pixels. If the voltage is large enough, neighboring pixels get triggered in addition to the original pixel. However, is the voltage lower than the THL, this information is lost, resulting in a loss of energy information. Graphic from [12].*

enough, the charge cloud can trigger neighboring pixels of the detector, leading to a spatial distribuiton of initial particle energy. Charge sharing can also lead to loss of energy information, when the energy in neighboring pixels is lower than the pixel threshold and triggering does not occur.

One significant difference between Timepix3 and Timepix is the clock design depicted in figure 2.5. Upon the output rising above the threshold, a discriminator indicates the voltage peak. The discriminator simultaneously starts a 640 MHz clock, measuring 'fine Time of Arrival' (fToA). The 640 MHz fToA clock stops at rising of a more coarse ToA clock with 40 MHz (in following denoted as 'sToA'). For the duration of the discriminator the ToT are counted synchronous to the ToA. A seperate 'Latch ToA' saves the first 40 MHz tick to relate the signal to a global ToA value. This global ToA gets translated into a pixel ToA, which proceeds to the read out for processing.

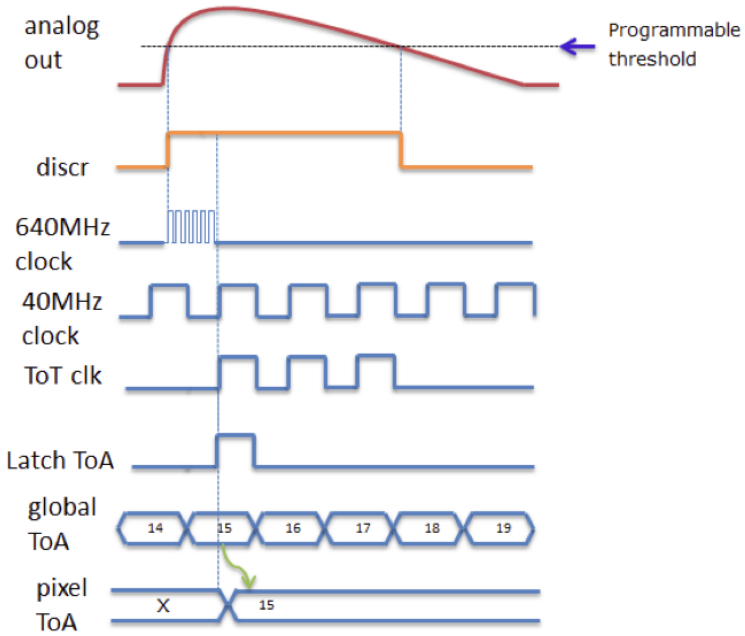

Figure 2.5: *Operation principle of a Timepix3 pixel. Upon detection of a voltage peak, several internal clocks are evaluated to determine ToT as well as ToA values. The number of 640 MHz clock ticks, the global number of 40 MHz clock tick on first tick during signal, and the number of ToT clock ticks during the signal get recorded. Figure taken from [10].*

This design allows for simultaneous measurement of ToA and ToT, additionally to a high resolution of time measurements. Since the fToA clock has a frequency of 640 MHz, the signal can be determined with an accuracy of 1.5625 ns.
After read out a pixel does experience a certain dead-time, in which the pixel cannot measure incoming signals. For Timepix3, the dead-time is 475 ns, compared to 300 μs for Timepix detectors. This dead-time however can increase when the chip operates near its maximum hit rate. In this work this effect was not observed, since the expected hit rate was comfortably below the maximum.

	Timepix	Timepix3
Pixels	256 × 256	256 × 256
Pixel size	55 μm	55 μm
Dead time per pixel	ToT pulse time + 475 ns	ToT pulse time + 300 μs

Table 2.2: *Comparison of Timepix and Timepix3 features [10] [11].*

2.3 Internal conversion

Upon decay Mn-54 has a $> 99\%$ chance to decay into an excited state of Cr-54. Similarly, Zn-65 posseses a 50.23% chance of decaying into an excited state of Cu-65. Upon deexcitation, both decay products emit a high energy photon. This gamma photon can interact with the remaining electron in the K-shell, exciting it into a higher shell or ionizing it completely from the atom. This process is called ' internal conversion ' and the ionized electrons are called ' conversion electrons '. Internal conversion leaves a fully vacant K-shell, similar to the process of double K-shell ionisation, however resulting from a distinctly different effect. To remedy this effect, it is possible to measure the ' conversion coefficient ' for the K-shell α_K and use it to correct the rate used for measuring P_{KK}. This correction is visible in equation 2.1, in which the conversion coefficient α_K gets substracted. For measurements according to equation 2.2 this correction is not necessary, since a 3-coincidence measurement includes the gamma photon. With an existing, non-interacting gamma photon, internal conversion is therefore impossible.
To measure the conversion coefficient in this work, following formula is used:

$$\alpha_K = \frac{N_{1KF1CE}}{TA\omega_K\omega_\gamma\delta_K\delta_{835e}} \tag{2.6}$$

N_{1KF1CE} describes the number of coincidences between one K-fluorescence photon and one conversion electron. δ_{835e} describes the detection efficiency of the conversion electrons.

3 Setup

To optimise data acquisition a modular experimental setup was designed. This allowed for the source to be quickly exchanged, while not changing the position of detectors in relation to the source. Figures 3.5 3.3 and 3.4 are showing a schematic overview of the experimental setup, as well as pictures of the source holder.
Data acquisition itself was achieved through the Kathrine readout developed by Burian [13]. As opposed to other Timepix readouts, Kathrine uses an Ethernet port to maximise readout speed and enable long range data acquisition for remote applications up to 100 meter. Kathrine saves the acquired data in form of an ASCII formatted .txt-File. In tabular form presented are: Pixel position, fToA, sToA and ToT of each registered pixel event.
To maximise the signal, two Timepix3 detectors were placed facing each other around the source. This allowed for maximal coverage of space angle while keeping the source at a low distance.
Multiple sources were measured and analysed. At time of measurement the Mn-54 source had an activity of 12249 Bq. The Zn-65 source had an activity of 8455 Bq. The Fe-55 source had an activity of 53825 Bq.
The usage of two detectors controlled by a Kathrine readout resulted in global offset of measurement time between the two detectors by 32 ns. This is due to the fact, that both detectors cannot be started at the exact same time down to a nanosecond. It is possible to correct this error during clustering (refer to 4.1). To establish the exact value of the offset, it is however necessary to leave this correction and analyze the data. The resulting effect is depicted in figures 3.1 and 3.2. Since only coincidences measured on both detectors result in a peak at 32 ns, the conclusion that a global offset between those detectors exist can be drawn. For further understanding of the method used in coincidence measurements, refer to section 4.4.

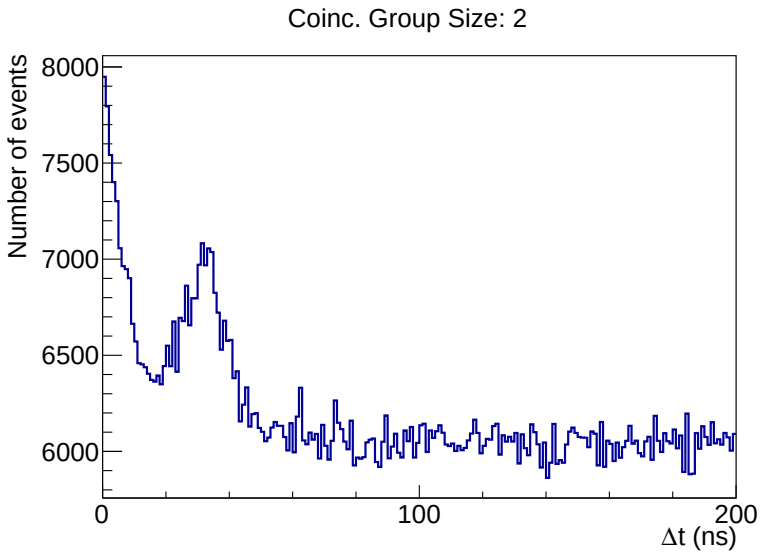

Figure 3.1: *Coincidence Times between two events of a Fe-55 source. A peak at 32 ns is visible, while the rest of the time spectrum, safe for the coincidence peak at the beginning, is flat.*

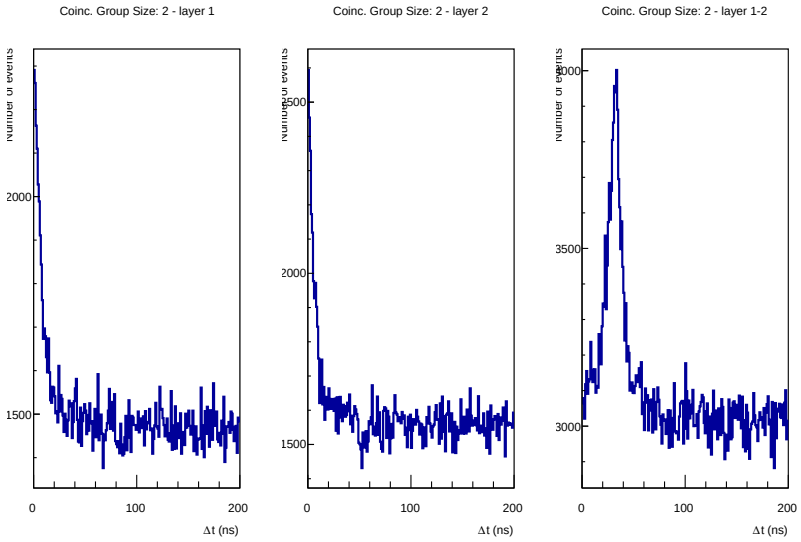

Figure 3.2: *Coincidence Times between two events of a Fe-55 source. The times are displayed in respect to different layers. The two lefthand graphes show the time distribution of events on one single detector, for each of the two detectors. The righthand graph depicts the time distribution of two events with each one occuring on one detector respectively. A peak at 32 ns is only visible in the righthand graph.*

Figure 3.3: *Containment for the sources used in the setup*

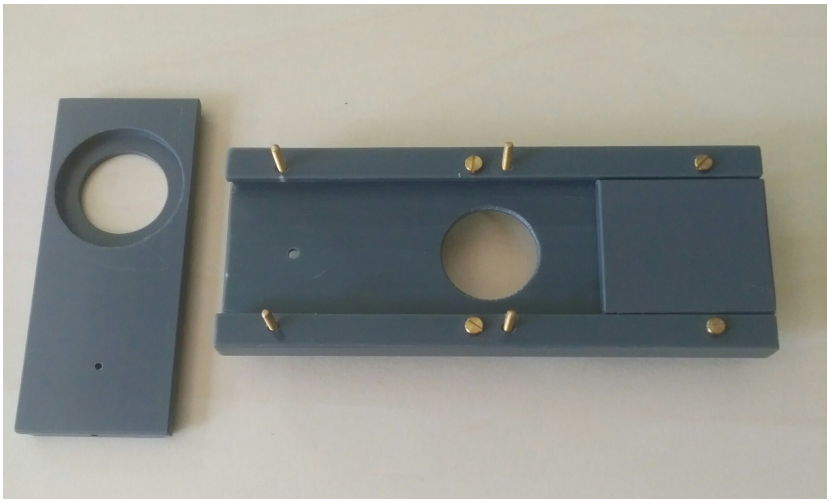

Figure 3.4: *Containment with source holder disassembled used in the setup*

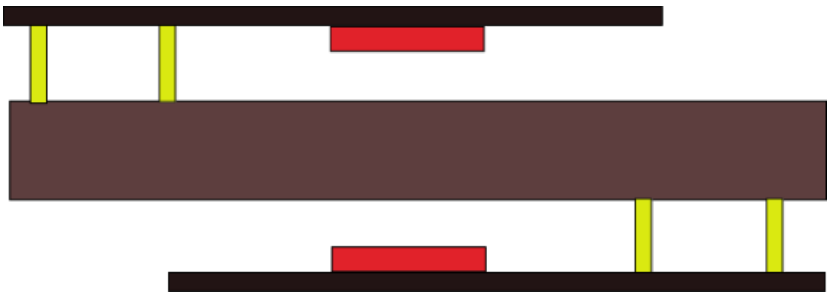

Figure 3.5: *Schematic depiction of the setup*

4 Analysis

4.1 Data processing

The first step for data analysis consisted of using a clustering program to process the ASCII data acquired by Kathrine. During process of clustering, the two files stemming from each of the two detectors are converted into one ROOT-Tree. Using the ROOT program by CERN it is then possible to analize the data.
During clustering several effects were already taken into consideration. One of the detectors used experienced an error during readout, leading to a shift of ToA values by 25ns in the pixel columns 181 and 182. A correction, applying a ToA-offset in those specific columns was applied during clustering. Furthermore there occured a slight delay between the detectors at measurement begin, resulting in a global ToA offset of 32ns between the respective files. A correction considering this offset was also taken into account. An energy calibration to convert ToT into energy measured in kiloelectronvolt was added during clustering.
After clustering the data, evaluation is possible through application of a ROOT-script.

4.2 Spatial distribution

It is possible to specifically look at the spatial distribution of events detected on the detectors. To achieve that a 256×256 pixelmatrix is filled with detected hits of both Timepix3, so the information of both detectors is shown on one matrix.
Depending on the source and acquisition time or quantity of recorded events, different pictures can be observed. In 4.1 the spatial distribution of events from a Mn-54 source in 6 hours is shown. The event count is concentrated in the middle of the detectors since the distance to the source is the lowest there. In 4.2 only the first 5000 recorded events of the environment of 4.1 are shown. Occasional electron tracks and single hits from K-Fluorescences or gamma particles are visible.

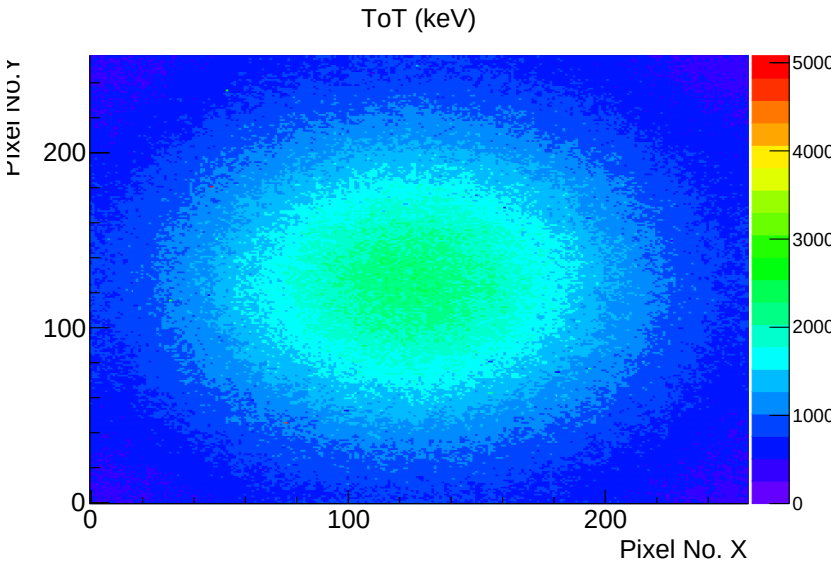

Figure 4.1: *Spatial Distribution of all events occuring from a Mn-54 source in 6 hours. The colour scale describes the deposited energy in each pixel over the course of measurement*

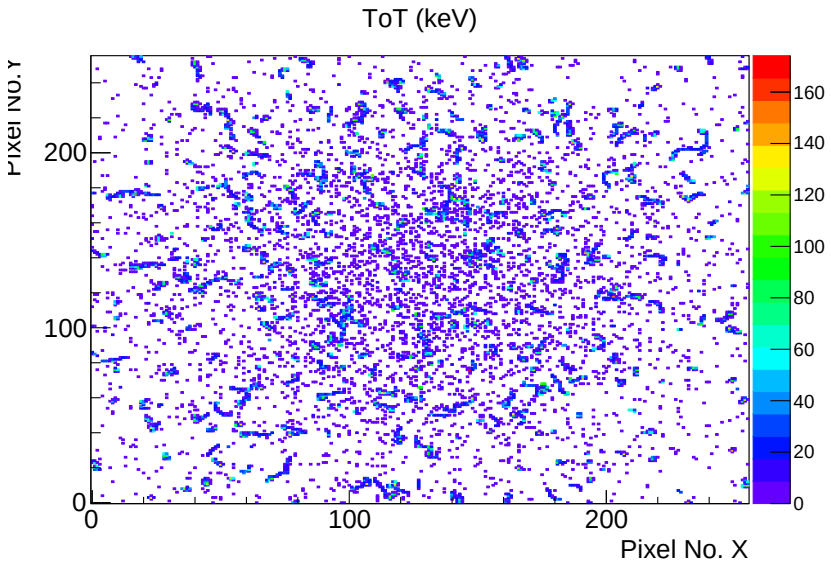

Figure 4.2: *Spatial Distribution of 5000 events occuring from a Mn-54 source. The colour scale describes the deposited energy in each pixel over the course of measurement*

4.3 Fluorescence, Gamma and Conversion electron count

To evaluate the conversion coefficients and P_{KK} the counts of K-Fluorescences, gamma particles and conversion electrons are necessary. The events were largely recognised by their energy signature. Since the energy ranges for the specific events change depending on the source material, everytime another source was observed the analysis was adjusted to account for those energies. In general some form of size cut was applied. Since charge sharing may distort results in low energy ranges, only single pixel events were counted as K-Fluorescences. For the electron tracks necessary for conversion electrons and gamma particles, an adequately high lower threshold was assumed for cluster size. For example, it is unlikely that an 835 keV electron track will only trigger 5 pixel, so only clusters consisting of more than 5 pixel were evaluated. The size cut was heuristically chosen as a means to filter crude possible errors from the result.

Event	Mn-54	Zn-65	Fe-55
K-Fluorescence	5.4 keV	8.0 keV	5.9 keV
Gamma transition	834.9 keV	1115.5 keV	$--$
Compton range	$<$ 600keV	$<$ 900 keV	$<$ 300 keV

Table 4.1: *Energy values of different events for the used elements. Fe-55 has a highly suppressed gamma transition. In this work, neither internal conversion, nor gamma transitions were observed for Fe-55. Values taken from [7] [8] and [9]. The Compton range is visible in section 5.1.*

4.4 Coincidence Measurements

For measurement of P_{KK} and α_K coincident events were evaluated. During the process of clustering, the events are grouped in ' coincidence groups '. A coincidence group consists of all events registered during a specific time period. During evaluation, coincidence groups can be analyzed to determine the number, distance and time difference of these coincident events, additionally to the usual energy, cluster and time information available for single events.
So for example, it is possible to only evaluate coincident events of one K-Fluorescence and two conversion electrons. Such a case is depicted in figure 4.3.

4.4.1 Time spectrum

A curious case can be observed by evaluating coincident events of any kind for the Mn-54 and Zn-65 sources. Even after global offset correction (see section 3) peaks in time distribution at around 30 ns can be observed. These distributions are depicted in figures 4.4 and 4.5.

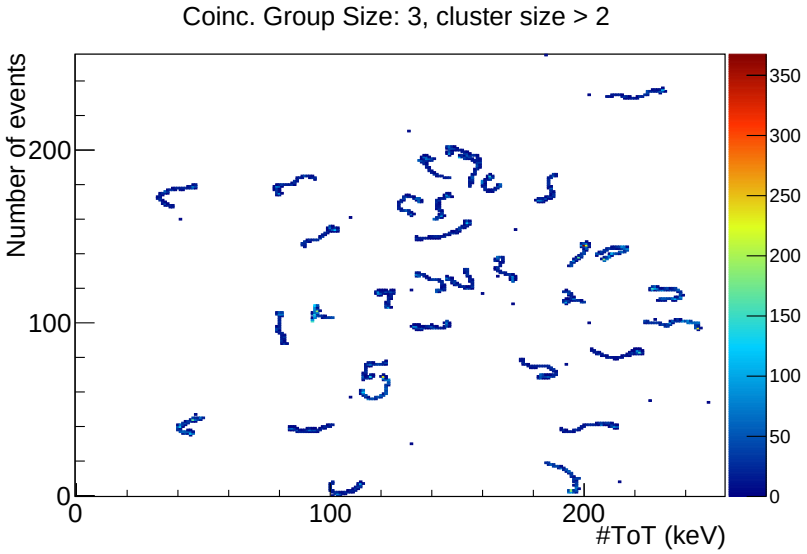

Figure 4.3: *Spatial Distribution of two coincident electron and K-Fluorescence events. Only 15 coincidence groups are plotted. The electrons are in the energy range of 800-870 keV, the K-Fluorescences are in the energy range of 1-12 keV.*

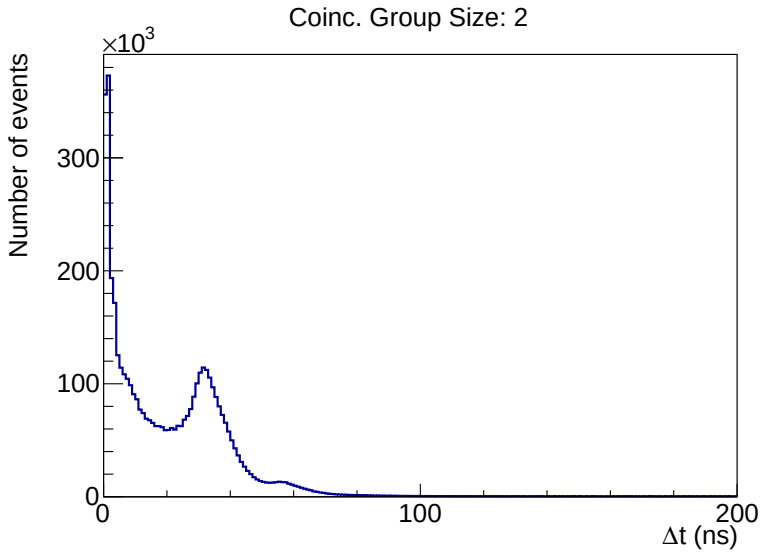

Figure 4.4: *Time distribution between two coincident events for the Mn-54 source. A peak at around 30 ns is distinctly visible.*

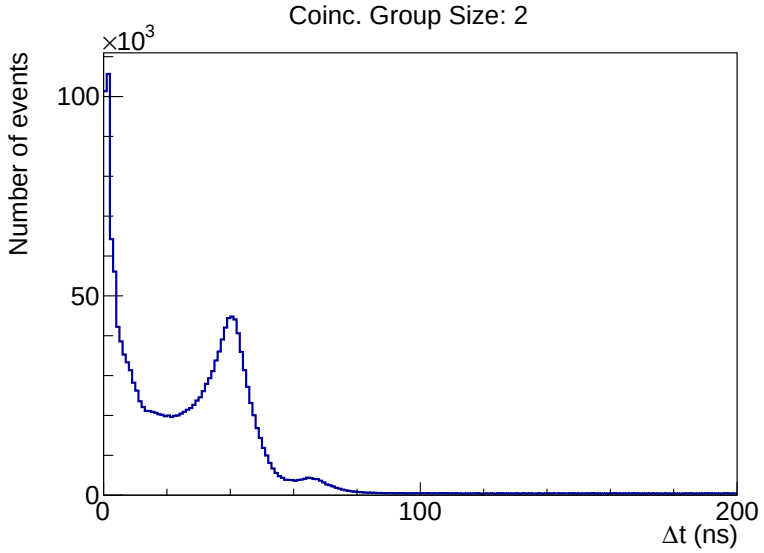

Figure 4.5: *Time distribution between two coincident events for the Zn-65 source. A peak at around 30 ns is distinctly visible.*

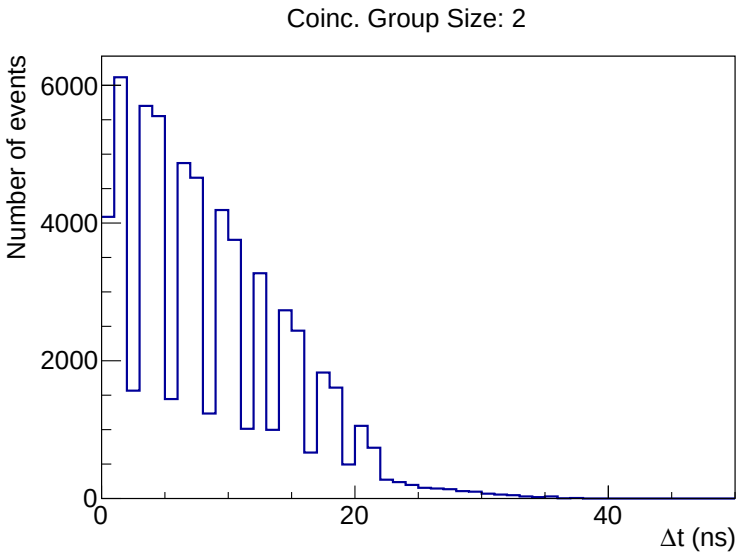

Figure 4.6: *Time distribution between two coincident events for a randomly simulated set of 100000 events. The distribution is evenly falling with dips every 2 ns. At 22 ns this effect disappears and the distribution stays flatly decreasing. These effects are most likely stemming from the simulation struggling with the calculation of time differences, taking sToA and fToA clocks into account. A peak at 30 ns however is not visible.*

Since time distributions for coincident events from Fe-65 do not experience this effect, a further time offset between the two detectors cannot be the cause.
To control if a faulty analysis might be the source of those peaks, a random set of data was simulated and analysed under the same procedure. As depicted in figure 4.6 a simulation using the TRandom3 generator of ROOT does not produce these 30 ns peaks.
Since the peak cannot be observed with the Fe-55 source (refer to figure 3.1), the effect might stem from conversion electrons emmitted at the gamma transition energy. To visualize this conclusion figures 4.7 and 4.8 depict a simulated detector response for Mn-54 conversion electrons and the energy distribution of coincident events during the 30 ns peak. In comparison to that, figure 4.9 depicts the energy distribution of coincident events during the first 20 ns of coincidence time. During the 30 ns peak, the energy distribution is peaking at 200 keV, before decreasing, akin to the simulated response of 835 keV electrons. An expected distribution of

energies, as depicted in 4.9 would show a compton edge and decrease at higher energies around 500 keV. Therefore it is plausible that those 835 keV conversion electrons are responsible for the 30 ns peak.
Another observed effect concerning the 30 ns peak is migration of the peak in relation to bias voltage. Figures 4.10 and 4.11 show the position of the peak in time spectrum at 150V and 230V bias. Considering the change of about 20ns between the two pictures, it is plausible that the bias voltage has an effect on the position of the peak.
To summarize the observations:

- A peak at about 30 ns occurs in the distribution of time differences for coincident events.
- This peak is only observed in measurements for Mn-54 and Zn-65.
- The peak is likely to be caused by high energy electrons in coincidence with low energy K-Fluorescences.
- The peak changes its position on the time spectrum in relation to bias voltage. Upon increase of bias voltage, the peak shifts to lower time differences and upon decrease of bias voltage the peak shifts to higher time differences.

These observations point to following explanation. Low energy photons are more likely to deposit their energy very near to the detector surface, as opposed to high energy events, which, if detected at all, are depositing their energy deep into the sensor layer. The difference in time is explained by a difference in drifttime for the created charge clouds necessary for detection. Since charge clouds ocurring from events near the sensor surface will have a longer way to drift to the electrodes of the detector than charge clouds from events near sensor bottom, they will also take a longer time. The detector will only measure a ToA upon arrival of charge clouds on the electrodes. This leads to an observed time difference equal to the difference in drift time, despite both ionizing events being emitted at the same time.
In this work, only Mn-54 and Zn-65 are able to emit high energy electrons and photons via gamma transition, so the effect is only visible for these two sources. Higher bias voltage leads to a faster migration of charge clouds, so the bias voltage will cause a change of observed position of the peak in the time spectrum.

4.4.2 Background

Not the whole 200ns window defined during the clustering process is used as a coincidence window. Significant coincidences are likely to occur in small window

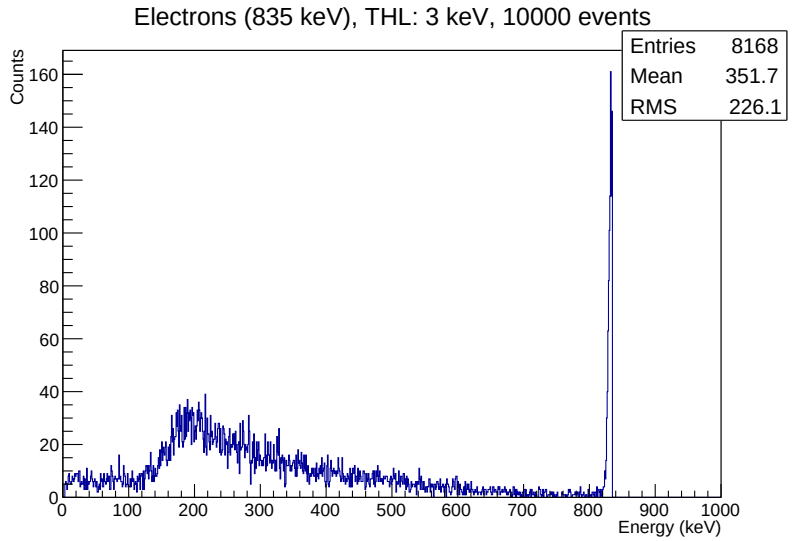

Figure 4.7: *Simulation of detector response for 835 keV electrons. Simulation and plot by [14].*

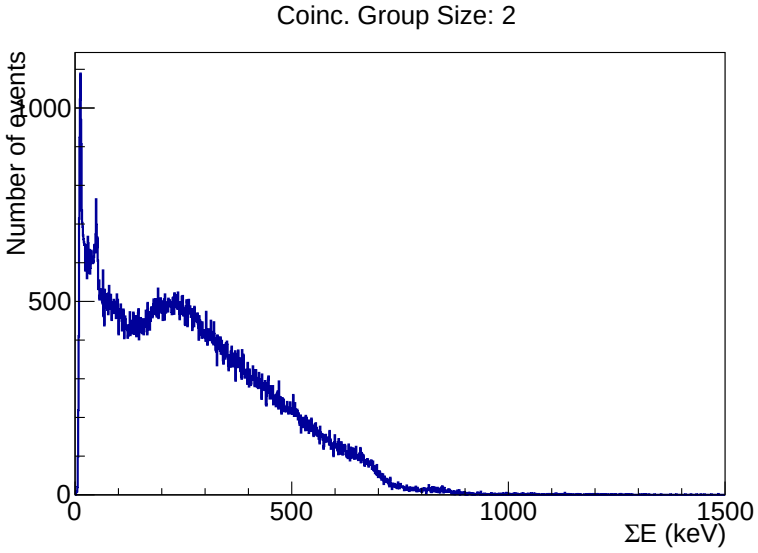

Figure 4.8: *Energy distribution of coincident events during the 30 ns peak of the Mn-54 source.*

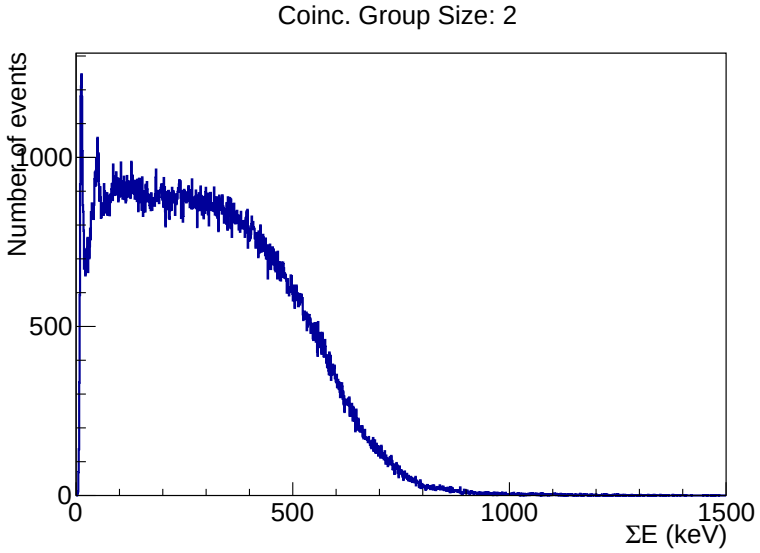

Figure 4.9: *Energy distribution of coincident events during the first 20 ns of coincidence time of the Mn-54 source.*

times, while with greater time differences, the coincidence being random is more likely. In this work consistently all events occuring within 20ns to each other are defined as coincidences. However, during this small time window a background of random coincidences is still possible. To determine the background resulting from random coincidences time spectra are observed. Specifically, another 20ns time window later in the time spectrum is evaluated. This random background reduction method is depicted in figure 4.12.
Furthermore, not only the temporal difference has an effect on the coincidence counts, but the spatial difference is important too. Figure 4.13 shows the distribution of distances between two coincident events. To determine this distance the mean x- and y-coordinates of coincident events werte taken, given the events were registered on the same detector. The distance between those events is then given as:

$$d(x_1, x_2, y_1, y_2) = \sqrt{(x_1 - x_2)^2 + (y_1 - y_2)^2} \tag{4.1}$$

For the purposes of this work, the unit was taken as pixels and not further converted into a length scale. Figure 4.13 shows a big count for small distances. This effect is

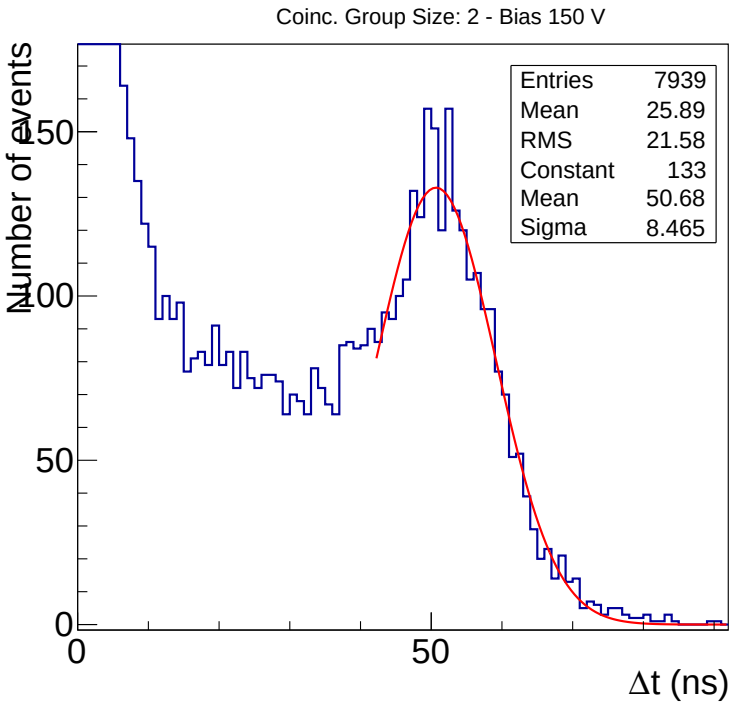

Figure 4.10: *Distribution of coincidence time differences for a measurement of Mn-54 with 150V bias voltage. The peak sits at roughly 50 ns. Plotted by [14].*

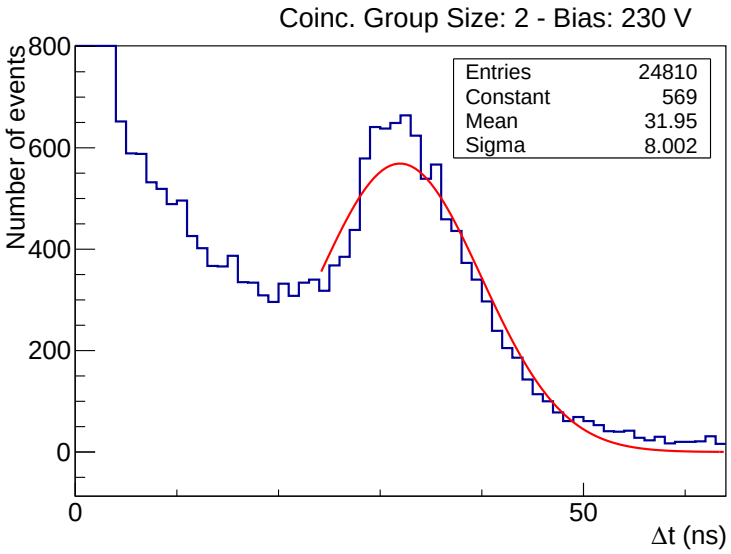

Figure 4.11: *Distribution of coincidence time differences for a measurement of Mn-54 with 230V bias voltage. The peak sits at roughly 30 ns. Plotted by [14].*

due to Compton scattering of ionizing particles depositing their energy in nearby pixels. It can happen that, due to this effect, those nearby hits, originatiing from one event, are registered as two seperate events. This effect does not depend on the source and has been observed for every coincidence measurement. To remedy this effect a cut on those low distances was introduced. On all coincidence measurements, coincidences with a spatial distance of less than 20 pixel were discarded.

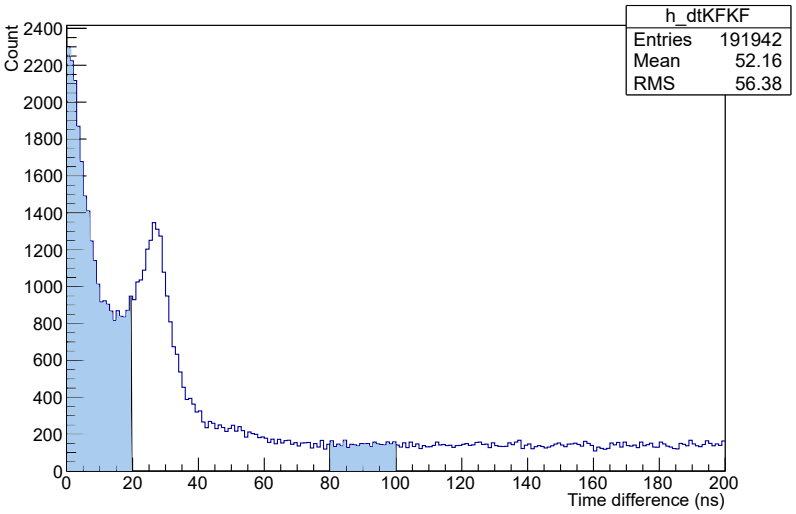

Figure 4.12: *Time differences between two coincident K-Fluorescences during 72 hours of measurement of Mn-54. The blue area between 0 ns and 20 ns denotes the events taken into consideration for analysis. The blue area between 80 ns and 100 ns was used to determine the random background. The peak at 30 ns is a fragment stemming from a faulty ToA correction during Clustering, mentioned in section 4.1.*

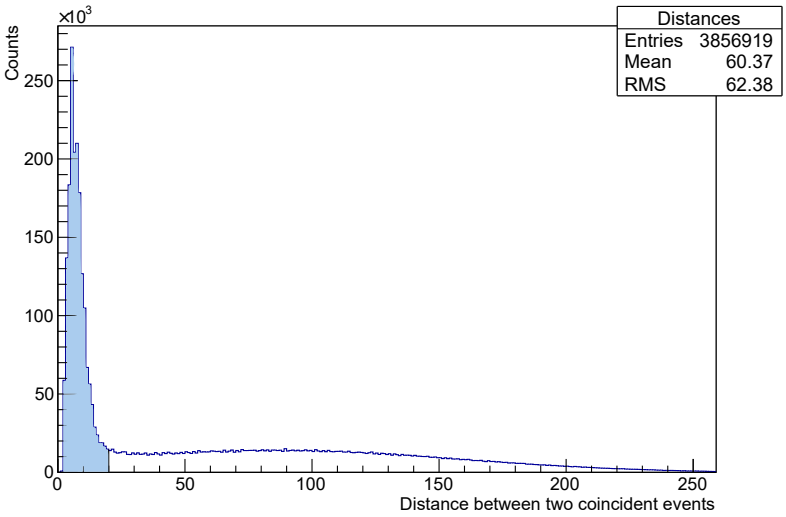

Figure 4.13: *Spatial distances of two coincident events in 126 hours of measurement of Mn-54. The blue area marks the cut applied to subsequent measurements. The distance was measured in pixel.*

5 Results

In this work, three sources were evaluated. Mn-54 was measured for 2581219 seconds or roughly 717 hours. Zn-65 was measured for 1634797 seconds or roughly 454 hours. Fe-55 was measured for 172979 seconds or roughly 48 hours. The directly measured data consisted of:

- x- and y-coordinates of pixel position
- ToT clock ticks during signal
- fToA clock ticks during signal
- sToA clock ticks during signal

This resulted in roughly 325 Gb of data to be analyzed according to section 4.

5.1 Energy distribution

The energy distribution of the sources are depicted in 5.1, 5.2 and 5.3. Notable in the spectra for Mn-54 and Zn-65 are the peaks at the respective gamma transition energies. The energy distribution for Mn-54 has a discernible peak at $835keV$, while the energy distribution for Zn-65 has one at $1115keV$.

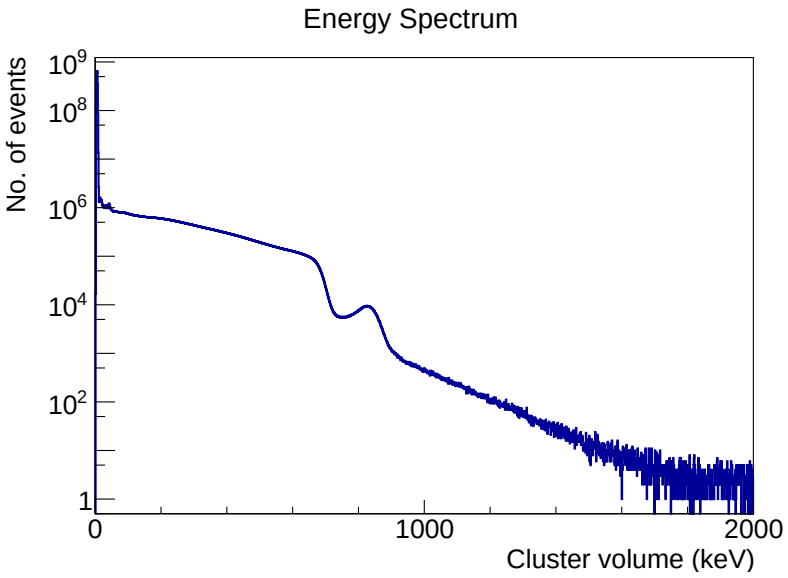

Figure 5.1: *Energy distribution of all measured events for the Mn-54 source. The measurement time was 2581219 seconds or roughly 717 hours.*

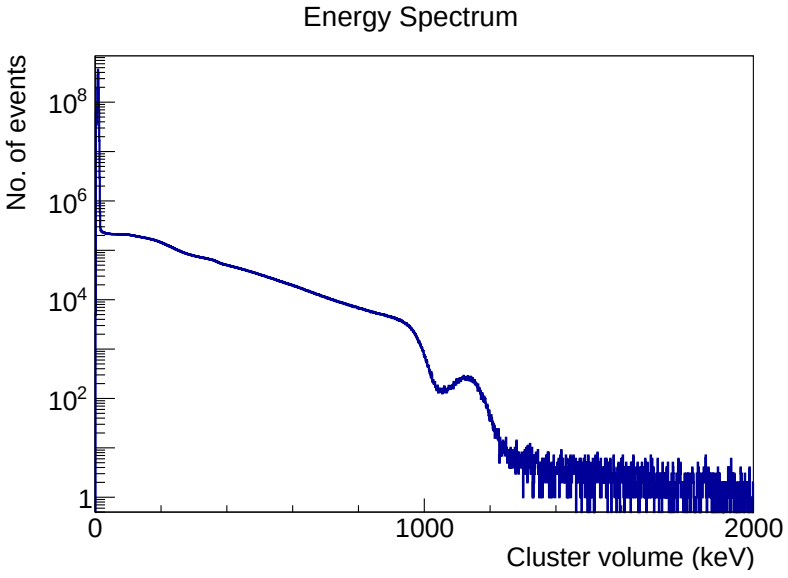

Figure 5.2: *Energy distribution of all measured events for the Zn-65 source. The measurement time was 1634797 seconds or roughly 454 hours.*

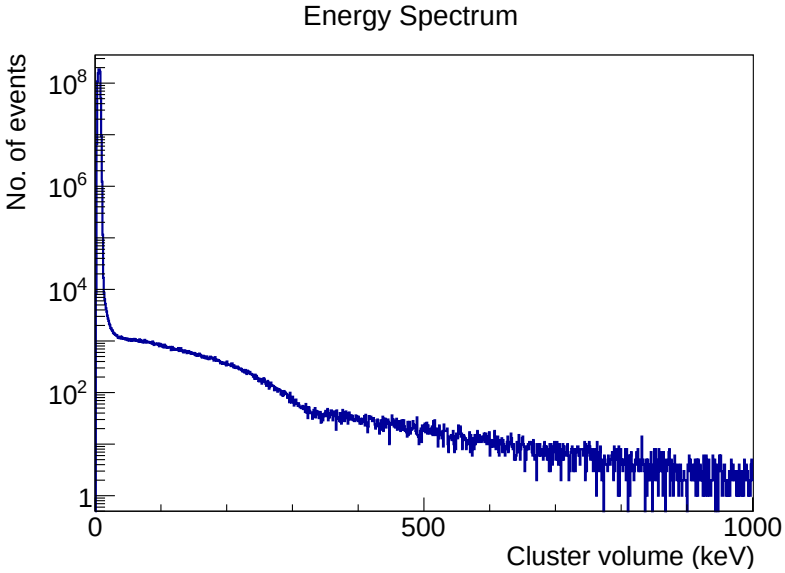

Figure 5.3: *Energy distribution of all measured events for the Fe-55 source. The measurement time was 172979 seconds or roughly 48 hours.*

5.2 Detector efficiency

To measure the detection efficiency δ_K of K-Fluorescences the count of K-Fluorescences N_K was evaluated with the formula:

$$\delta_K = \frac{N_K}{TA\omega_K} \tag{5.1}$$

The values for δ_{HS} and δ_S cannot be directly measured, since the energy difference between hypersatellites/satellites and K-Fluorescences is smaller than the resolution of the Timepix3. However, strictly speaking, the efficiencies of those are different to the efficiency of normal K-Fluorescences. To describe a more accurate value, the following ratios are assumed [2]:

$$K_{HS} = \frac{\delta_{HS}}{\delta_K} = 1.0499; K_S = \frac{\delta_S}{\delta_K} = 1.0118 \tag{5.2}$$

In this work these ratios, measured for a similar setup using Timepix-Detectors for measurements with Fe-55, are also applied to the measurements with Mn-54 and Zn-65. Since the energy difference between hypersatellites, satellites and K-

δ	Mn-54	Zn-65	Fe-55
δ_K	0.289	0.340	0.316
δ_S	0.293	0.344	0.319
δHS	0.304	0.357	0.331
δ_γ	0.0076	0.0049	$--$

Table 5.1: *Detection efficiencies for Mn-54, Zn-65 and Fe-55*

Fluorescences are consistently on a scale of only a few hundred meV, the Timepix3 wont have a difference in detection efficiency, compared to measurements with Fe-55.
Using those values the efficiencies are calculated to:

5.3 Conversion coefficients

To measure the conversion coefficients for Mn-54 and Zn-65, measurements of two coincident events, one K-Fluorescence and one conversion electron were taken. Evaluation happened according to equation 2.6. It is notable that ω_γ is very different between Mn-54 and Zn-65:

$$\omega_{\gamma,Mn54} = 0.999997; \omega_{\gamma,Zn65} = 0.5023 \tag{5.3}$$

Measurements of the sources used in this work yielded conversion coefficients of $\alpha_K = 1.99 \pm 0.009 \times 10^{-4}$ for Mn-54 and $\alpha_K = 2.68 \pm 0.068 \times 10^{-5}$ for Zn-65. The α_K for Mn-54 is therefore with our measurement 10 % lower than the value from literature [7] ($\alpha_K = 2.22 \times 10^{-4}$). The α_K for Zn-65 is a magnitude below the value in literature [8] ($\alpha_K = 1.66 \times 10^{-4}$). Since these values are used according to equation 2.1 during calculation of P_{KK}, in following the literature values are used. For a discussion of the disparity between the measurement here and literature, refer to section 6.

5.4 P_{KK} values

In this section, specifically in the table below, the final results for the P_{KK} for each of the three sources and two methods are presented. A measurement with

P_{KK}	Mn-54	Zn-65	Fe-55
$P_{KK,2C}$	$6.38 \pm 0.03 \times 10^{-4}$	$2.32 \pm 0.01 \times 10^{-4}$	$1.38 \pm 0.04 \times 10^{-4}$
$P_{KK,3C}$	$2.86 \pm 0.21 \times 10^{-4}$	$5.46 \pm 0.23 \times 10^{-4}$	–

Table 5.2: *P_{KK} for Mn-54, Zn-65 and Fe-55. $P_{KK,2C}$ denotes the results of the measurement method with two coincident K-Fluorescences. $P_{KK,3C}$ denotes the results of the measurement method with three coincidences, two K-Fluorescences and one gamma photon. $P_{KK,3C}$ cannot apply to Fe-55, since no gamma photon is emitted.*

three coincident events was not conducted for Fe-55, since no gamma transition took place. The values were calculated according to equations 2.1 and 2.2.

6 Discussion

There are a few remarkable points following those results. Upon comparing the P_{KK} values measured in this work to previous measurements, it is not clear which method works best. While measurement of two coincident events for Zn-65 delivers a result in agreement with Nagy [15], the measurement of three coincident events is larger by a factor of 2. Furthermore, the opposite case is found in Mn-54, where measurement of three coincident events is included in the margin of error with Hindi [1], while measurement with two coincident events are also roughly larger by a factor of 2. The only clear case is the measurement of Fe-55, which is in agreement with previous measurements by Michel [5]. This points to the fact that, while it is possible using Timepix3 detectors to measure P_{KK}, problems and uncertainties will arise when observing sources undergoing gamma transition. This fact gets further confirmed by the measurement of the conversion coefficient α_K for Zn-65. While α_K for Mn-54 only differs by 10 % of the literature value, Zn-65 is differing by a factor of 20. The reason for that difference most likely lies in the different decay modes of Zn-65 compared to Mn-54. While Mn-54 mostly has one gamma transition occuring every decay [7], Zn-65 has three different gamma transition possibilities with varying probabilities. A gamma transition for Zn-65 is not guaranteed upon decay [8]. This can impose an unknown error on the measurement of α_K, and can further complicate a coincidence measurement using gamma photons.

Another aspect of complication were the multiple time offsets experienced during setup, tests and measurements. The difficulty of exactly starting both detectors at the same nanosecond, the ToA offset caused by electrical problems within the detector and the shift of coincidence times caused by physical effects within the detector all resulted in unexpected time difference distributions for coincident events. The fact that some of those effects gave time inaccuracies of roughly the same value caused a sub-optimal environment for coincidence measurements. These effects might be supressed by using a possible future generation of Timepix detector.

The question of the true dependence of P_{KK} to the atom number Z remains with these results. A disparity this large in P_{KK} between the sources Mn-54, Fe-55 and Zn-65 cannot be explained by a power law like in figure 2.1. This holds for the results of this work, as well as for previous measurements by other bodies [5] [1] [15].

7 Summary

In this work it was shown, that the Timepix3 detector can be a viable tool for detection of P_{KK} given the right element. However, measurements using three coincident events, for example to apply a veto on processes with similar energy signature, especially if gamma transition is involved, do not guarantee feasible results. These cases require a sophisticated approach to analyze coincidence results. After measurements on three different sources with the Timepix3 the disparity in theoretical values and measurements of P_{KK} could not be resolved.
To improve measurements on sources involving gamma transition, a coupling of the Timepix3 detector to measure K-Fluorescences and hyper/-satellites, and an external detector to reliably measure gamma photons, could be possible.

Bibliography

[1] M. M. Hindi, C. A. White, and R. L. Kozub. Double k-shell ionization probability in ^{54}Mn. *Phys. Rev. C*, 68:014306, Jul 2003.

[2] Benedikt Bergmann, Thilo Michel, Andrey Surzhykov, and Stephan Fritzsche. Angular correlation function of the hypersatellite-satellite x-ray cascade following k-shell electron capture of ^{55}Fe. *Phys. Rev. C*, 94:014611, Jul 2016.

[3] J. L. Campbell, J. A. Maxwell, and W. J. Teesdale. Double k-shell ionization in the electron capture decay of ^{55}Fe. *Phys. Rev. C*, 43:1656–1663, Apr 1991.

[4] H. Primakoff and F. T. Porter. Atomic excitation and ionization accompanying orbital electron capture by nuclei. *Phys. Rev.*, 89:930–937, Mar 1953.

[5] Thilo Michel, Benedikt Bergmann, Jürgen Durst, Mykaylo Filipenko, Thomas Gleixner, and Kai Zuber. Measurement of the double k-shell vacancy creation probability in the electron-capture decay of ^{55}Fe with active-pixel detectors. *Phys. Rev. C*, 89:014609, Jan 2014.

[6] E. P. Kanter, I. Ahmad, R. W. Dunford, D. S. Gemmell, B. Krässig, S. H. Southworth, and L. Young. Double k-shell photoionization of silver. *Phys. Rev. A*, 73:022708, Feb 2006.

[7] LNE LNHB/CEA Mn-54, Table of Radionucleids. `http://www.nucleide.org/DDEP_WG/DDEPdata.htm`. called on 20.08.2018.

[8] LNE LNHB/CEA Zn-65, Table of Radionucleids. `http://www.nucleide.org/DDEP_WG/DDEPdata.htm`. called on 20.08.2018.

[9] LNE LNHB/CEA Fe-55, Table of Radionucleids. `http://www.nucleide.org/DDEP_WG/DDEPdata.htm`. called on 20.08.2018.

[10] T Poikela, J Plosila, T Westerlund, M Campbell, M De Gaspari, X Llopart, V Gromov, R Kluit, M van Beuzekom, F Zappon, V Zivkovic, C Brezina, K Desch, Y Fu, and A Kruth. Timepix3: a 65k channel hybrid pixel readout chip with simultaneous toa/tot and sparse readout. *Journal of Instrumentation*, 9(05):C05013, 2014.

[11] X. Llopart, R. Ballabriga, M. Campbell, L. Tlustos, and W. Wong. Timepix, a 65k programmable pixel readout chip for arrival time, energy and/or photon

counting measurements. *Nuclear Instruments and Methods in Physics Research A*, 581:485–494, October 2007.

[12] J Jakubek. Semiconductor Pixel detectors and their applications in life sciences. *J. Instrum.*, 4:P03013, 2009.

[13] P. Burian, P. Broulím, M. Jára, V. Georgiev, and B. Bergmann. Katherine: Ethernet embedded readout interface for timepix3. *Journal of Instrumentation*, 12(11):C11001, 2017.

[14] Correspondence with Benedikt Bergmann, MSc.

[15] H. J. Nagy and G. Schupp. Double k-shell ionization in the electron capture decays of ^{65}Zn. *Phys. Rev. C*, 27:2887–2892, Jun 1983.

Acknowledgements

First and foremost, i am thankful to Dr Thilo Michel, who always helped me out when a problem occured and was quick to give advise. A few words can go a long way to calm a mind.
I thank Benedikt Bergmann. His groundwork made this work possible and without his thoughts and input, i might have been lost a few times.
I like to thank my colleagues in office. D A M M F N T P J S always produced the most comfortable atmossphere.
I thank the IEAP Prague and the Faculty of Electrical Engineering Pilsen for providing detector, readout, delivery and commissioning.
I thank Prof Gisela Anton for the opportunity to produce this thesis.
I thank my parents for providing me all the support i needed during this time.
At last, I thank my dear sister.

Erklärung

Hiermit versichere ich, dass ich diese Masterarbeit selbständig verfasst und keine anderen als die angegebenen Quellen und Hilfsmittel benutzt habe. Die Stellen meiner Arbeit, die dem Wortlaut oder dem Sinn nach anderen Werken entnommen sind, habe ich in jedem Fall unter Angabe der Quelle als Entlehnung kenntlich gemacht. Das selbe gilt sinngemäß für Tabellen und Abbildungen. Diese Arbeit hat in dieser oder einer ähnlichen Form noch nicht im Rahmen einer anderen Prüfung vorgelegen.

Erlangen, den 27. 8. 2018

Daniel Voigt